American Journal of Applied Chemistry
2026, Vol. 14, No. 4, pp. 62–71
https://doi.org/10.11648/j.ajac.20261404.11

SciencePG
Science Publishing Group

Research Article

Efficient Photocatalytic Rhodamine B Dye Degradation Using Activated Carbon-Based TiO_2 Photocatalyst

Sagar Kande*

Department of Chemistry, New Arts, Commerce and Science College, Shevgaon, India

Abstract

Environmental contamination caused by synthetic dye effluents from the textile, paper, and printing industries poses severe ecological threats. In this work, a highly efficient activated carbon-based titanium dioxide (AC-TiO_2) composite photocatalyst was successfully synthesized via a modified sol-gel route for the targeted degradation of Rhodamine B (RhB) dye under simulated solar irradiation. The synthesized materials were comprehensively characterized using X-ray Diffraction (XRD), Field Emission Scanning Electron Microscopy (FE-SEM) coupled with Energy Dispersive X-ray Spectroscopy (EDS), Transmission Electron Microscopy (TEM), Fourier Transform Infrared Spectroscopy (FTIR), UV-Vis Diffuse Reflectance Spectroscopy (UV-Vis DRS), X-ray Photoelectron Spectroscopy (XPS), and Brunauer-Emmett-Teller (BET) surface area analysis. XRD confirmed the formation of highly crystalline anatase-phase TiO_2, while BET analysis revealed that the integration of activated carbon drastically enhanced the specific surface area from 52.4 m^2/g (pure TiO_2) to 284.7 m^2/g (AC-TiO_2). UV-Vis DRS displayed a prominent red shift in the absorption edge of the composite, effectively narrowing the band gap energy from 3.20 eV to 2.85 eV, enhancing light absorption in the visible range. Photocatalytic performance evaluation showed that the AC-TiO_2 composite achieved a superior RhB degradation efficiency of 98.5% within 60 minutes of irradiation, significantly outperforming benchmark Aeroxide P25 (71.2%) and pure TiO_2 (63.4%). Kinetic analysis revealed that the degradation followed a pseudo-first-order mechanism, with a rate constant ($k = 0.0681\ min^{-1}$) that is ~ 4.3 times higher than pristine TiO_2. The synergistic mechanism is attributed to the dual role of activated carbon as an exceptional adsorptive sink and an electron trapping mediator that effectively retards the recombination of photogenerated electron-hole (e^-/h^+) pairs. Furthermore, scavenger experiments confirmed that hydroxyl radicals ($^{\bullet}OH$) and superoxide radical anions ($^{\bullet}O_2^-$) acted as the dominant reactive oxygen species driving the mineralisation process. The composite displayed excellent reusability, maintaining a 92.1% degradation efficiency after five consecutive cycles, demonstrating high stability. This study highlights the potential of AC-TiO_2 composites as an eco-friendly, cost-effective, and highly viable candidate for high-throughput industrial wastewater remediation.

Keywords

Heterogeneous Photocatalysis, Titanium Dioxide, Activated Carbon, Rhodamine B, Synergistic Degradation, Water Treatment

1. Introduction

Rapid global industrialization, particularly in the textile, leather, cosmetics, and plastics manufacturing sectors, has led to an exponential increase in the discharge of hazardous wastewater containing synthetic organic dyes into natural water bodies [1-4]. Among these pollutants, Rhodamine B (RhB) is a highly water-soluble, synthetic cationic dye belonging to

*Correspondence: Sagar Kande (srkande87@gmail.com)

Received: 28 July 2026; **Accepted:** 10 August 2026; **Published:** 27 August 2026

the xanthene class. It is widely applied as a colorant and biomarker but represents a major environmental hazard due to its neurotoxicity, carcinogenicity, mutagenicity, and structural stability against natural biodegradation [5]. When introduced into aquatic ecosystems, RhB drastically reduces light penetration, severely impeding photosynthetic activity and disrupting the primary biological food chain. Conventional treatment paradigms-including physical coagulation, flocculation, membrane filtration, air stripping, and adsorption-merely transfer the pollutants from the aqueous phase to a solid concentrated sludge phase, generating secondary pollution that demands expensive post-treatment procedures [6, 7].

To address these drawbacks, Advanced Oxidation Processes (AOPs), and specifically heterogeneous semiconductor photocatalysis, have emerged as a sustainable, cost-effective, and environmentally benign technology capable of completely mineralizing recalcitrant organic contaminants into harmless end products such as water, carbon dioxide, and dilute mineral acids [8-10]. Among a myriad of oxide semiconductor photocatalysts investigated, Titanium Dioxide (TiO_2) remains the preeminent benchmark candidate owing to its strong oxidizing potential, chemical durability, low toxicity, abundance, and resistance to photocorrosion. However, the widespread industrial application of pristine TiO_2 is strictly bottlenecked by two fundamental thermodynamic limitations: (i) a wide intrinsic bandgap (~3.20 eV for anatase), which confines its photoactivation to the narrow ultraviolet (UV) region comprising only 4-5% of the solar spectrum, and (ii) an rapid recombination rate of photogenerated electron-hole pairs (e^-/h^+), which dramatically lowers the quantum efficiency [11, 12].

To circumvent these limitations, strategic modifications such as metal/non-metal doping, semiconductor heterojunction engineering, and carbonaceous material hybridization have been extensively developed [13]. Among carbon-based supports, Activated Carbon (AC) stands out as a highly attractive matrix due to its massive specific surface area, well-developed hierarchical porosity (microporous, mesoporous, and macroporous network), chemical inertness, and exceptional adsorption capacity. Hybridizing TiO_2 with activated carbon yields a highly potent synergistic mechanism [14, 15]. The high adsorption affinity of AC rapidly concentrates RhB molecules around the active catalytic centers of TiO_2, creating an enriched reaction zone. Simultaneously, oxygen-containing functional groups and localized graphitic sp^2 domains within the activated carbon act as excellent electron sinks, capturing photo-excited electrons from the conduction band of TiO_2, thereby suppressing electron-hole recombination and dramatically amplifying the photocatalytic efficiency under solar light [16-19].

In this comprehensive study, an advanced, highly efficient activated carbon-based TiO_2 composite (AC-TiO_2) was synthesized via a precise, low-temperature sol-gel method. The chemical architecture, morphological attributes, optical profiles, electrical state parameters, and porous networks were thoroughly interrogated using advanced characterization frameworks (XRD, FESEM-EDS, TEM, FTIR, UV-Vis DRS, XPS, and BET). The photocatalytic activity was evaluated by tracking the degradation of RhB under simulated solar irradiation, followed by exhaustive optimization of key operational variables, kinetics modeling, scavenger trapping studies, and recyclability assessments. Based on these observations, a detailed dual-functional adsorption-photocatalysis synergistic mechanism is presented, establishing the operational validity of this composite system for industrial wastewater remediation.

2. Experimental Section

2.1. Materials and Chemicals

Titanium tetraisopropoxide (TTIP, 97% purity), Rhodamine B (RhB, analytical grade, >=99%), isopropyl alcohol (IPA), absolute ethanol, ammonium oxalate (AO), benzoquinone (BQ), and analytical grade nitric acid (HNO_3) were procured from Sigma-Aldrich and used without further purification. Activated carbon (AC) derived from coconut shells was obtained from local chemical suppliers, thoroughly washed with 0.1 M HCl and deionized (DI) water, dried at 105°C for 12 hours, and milled to a fine mesh size prior to synthesis. High-purity deionized water was strictly deployed throughout all solution preparation and washing protocols.

2.2. Synthesis of AC-TiO_2 Composite Photocatalyst

The AC-TiO_2 composite was prepared via a controlled sol-gel methodology. In a typical procedure, 10 mL of TTIP was dissolved in 40 mL of absolute ethanol under vigorous magnetic stirring for 30 minutes to form Solution A. Separately, Solution B was prepared by mixing 10 mL of ethanol, 2 mL of deionized water, and 1.5 mL of a 2M HNO_3 solution (acting as a peptizing and acid-catalyst agent). Solution B was then added dropwise to Solution A over a period of 45 minutes under continuous high-speed stirring (700 rpm) at room temperature to initiate controlled hydrolysis. Once a homogeneous translucent sol was achieved, a predetermined mass of pretreated activated carbon (calculated to yield a optimal 5 wt.% carbon loading in the final product) was slowly introduced into the gel matrix. The mixture was continuously stirred for another 3 hours to guarantee absolute uniformity. The resulting composite gel was aged at ambient conditions for 24 hours, subsequently dried in a vacuum oven at 80°C for 12 hours to eliminate residual volatile solvents, and finally calcined in a programmable muffle furnace under an inert nitrogen atmosphere at 450°C for 3 hours (heating ramp rate of 2°C/min). For comparative baseline indexing, pristine TiO_2 was synthesized via an identical protocol omitting the addition of activated carbon.

2.3. Material Characterization Framework

Using a Cu Kα radiation source at 40 kV and 30 mA across a 2θ range of 10-80º, the Brucker D8 Advance diffractometer was used to get the powder X-ray diffraction pattern of manufactured photocatalysts. The Renishaw InVia Raman spectrometer was used to obtain the Raman spectra. The produced photocatalyst's morphology was examined using EDX on a Bruker XFlash 6I30 and scanning electron microscopy (SEM) on a Nova NanoSEM 450. The high resolution transmission electron microscope (HRTEM) and selected area electron diffraction (SAED) pictures are obtained from FEI Tecnai F30 TEM. ESCA-3000, VG Microtech, Uckfield, UK, was used to assess the binding energy and chemical state. Photoluminescence (PL) spectra were collected on SCINCO Fluoro Mate FS-2. The PE LAMBDA35 spectrophotometer was used to acquire diffuse reflectance spectra. The Brunauer-Emmett-Teller (BET) specific surface area measurement was carried out by N_2 adsorption/desorption at 77K utilizing Micrometrics ASAP 2020 devices.

2.4. Photocatalytic Activity Evaluation

The photocatalytic performance of the AC-TiO_2 composite was evaluated by monitoring the degradation of RhB under simulated solar light illumination using a 300W Xenon lamp equipped with a UV cut-off filter (λ >= 420 nm). In each standard evaluation, 50 mg of the selected photocatalyst was dispersed into 100 mL of an aqueous RhB dye solution (initial concentration C_0 = 20 mg/L). Prior to turning on the light, the suspension was stirred vigorously in the dark for 30 minutes to establish complete adsorption-desorption equilibrium between the dye molecules and the catalyst surface. The system was maintained at a constant temperature of 25°C using a circulating water cooling jacket. Under light exposure, aliquots of 3 mL were drawn from the reaction cell at regular 10-minute intervals over a total span of 60 minutes. The collected samples were centrifuged immediately at 10,000 rpm for 5 minutes to fully remove catalyst particles. The residual concentration of RhB was determined by measuring the maximum absorbance at λ_{max} = 554 nm using a UV-Vis spectrophotometer. The degradation efficiency (%) was computed using the relation:

$$\text{Degradation Efficiency (\%)} = [(C_0 - C_t) / C_0] \times 100 \quad (1)$$

where C_0 represents the initial equilibrium concentration after dark adsorption, and Ct is the concentration at irradiation time t. as shown in the equation (1). To identify the primary reactive species involved, trapping experiments were conducted using isopropyl alcohol (IPA, 10 mM), benzoquinone (BQ, 2 mM), and ammonium oxalate (AO, 10 mM) as specific scavengers for hydroxyl radicals (•OH), superoxide radicals ($\bullet O_2^-$), and photogenerated holes (h^+), respectively.

3. Results and Discussion

3.1. X-ray Diffraction (XRD) Analysis

The crystalline structure and phase composition of pure AC, pristine TiO_2, and the AC-TiO_2 composite were systematically evaluated via XRD, as illustrated in the experimental records. The XRD pattern of pure AC shows a broad, low-intensity reflection peak centered near 2θ = 24.5°, corresponding to the (002) reflection plane of amorphous carbon architectures. For the pristine TiO_2 sample, high-intensity, sharp diffraction peaks are clearly visible at 2θ values of 25.3°, 37.8°, 48.0°, 53.9°, 55.1°, 62.7°, 68.8°, 70.3°, and 75.1°. These reflections correspond to the (101), (004), (200), (105), (211), (204), (116), (220), and (215) crystallographic planes, aligning perfectly with the standard tetragonal anatase phase of TiO_2 (JCPDS card no. 21-1272). No diffraction peaks matching the rutile or brookite polymorphs were detected, indicating high phase purity. For the AC-TiO_2 composite, all characteristic reflections of the anatase phase remain dominant, demonstrating that the structural framework of TiO_2 was not altered during the composite synthesis or calcination step. The amorphous carbon reflection peak (24.5°) is completely obscured by the intense (101) anatase reflection located at 25.3°. The average crystallite size was calculated using Scherrer's equation based on the full-width at half-maximum (FWHM) of the prominent (101) peak. Shown in the equation (2).

$$D = (K * \lambda) / (\beta * \cos(\theta)) \quad (2)$$

The calculated average crystallite size for pristine TiO_2 was 18.4 nm, whereas the AC-TiO_2 composite exhibited a slightly smaller crystallite size of 15.2 nm. This minor decrease suggests that the highly dispersed activated carbon framework acts as a physical barrier during the sol-gel process, effectively retarding the agglomeration and grain growth of TiO_2 nanoparticles during high-temperature calcination [20, 21].

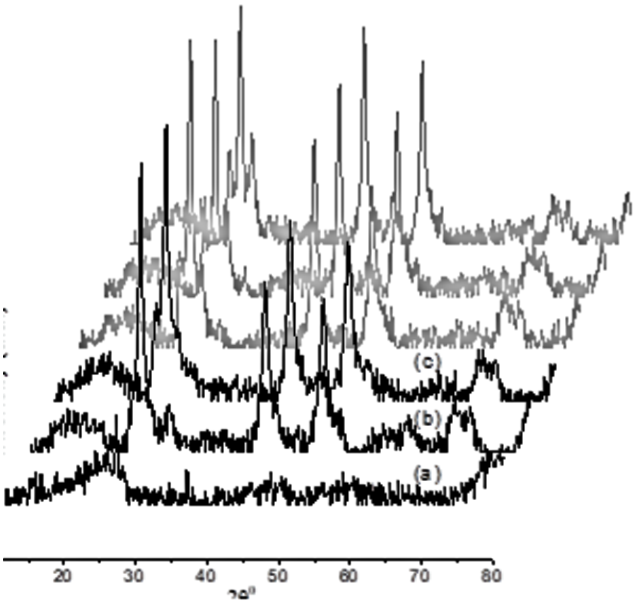

Figure 1. *X-ray Diffraction pattern of prepared photocatalysts a) Pure AC, b) Pristine TiO_2 and c) AC-TiO_2 Composite.*

3.2. Morphological and Microstructural Analysis (FE-SEM & TEM)

FE-SEM imaging reveals that pristine TiO_2 synthesized without a carbon support forms highly agglomerated, irregular spherical clusters due to its high surface energy. In contrast, the FE-SEM micrographs of the AC-TiO_2 composite display a completely different morphology. Here, the activated carbon matrix acts as an expansive, highly porous backbone, across which ultra-fine TiO_2 nanoparticles are uniformly anchored and distributed. This structured dispersion significantly mitigates particle agglomeration, exposing a larger number of active catalytic sites. Energy Dispersive X-ray Spectroscopy (EDS) elemental mapping confirms the highly uniform co-existence of Titanium (Ti), Oxygen (O), and Carbon (C) across the composite matrix, with no external impurities detected, confirming the success of the synthesis process [22, 23].

TEM and HR-TEM analyses provide deeper insights into the interfacial architecture of the composite. TEM images show that the TiO_2 nanoparticles, with diameters ranging from 12 to 18 nm, are securely attached to the smooth, thin sheets of the activated carbon matrix. This direct integration is crucial for fast interparticle charge transfer. The HR-TEM image clearly reveals well-defined, continuous lattice fringes with an interplanar d-spacing of 0.352 nm, which corresponds perfectly to the (101) lattice plane of anatase TiO_2 [24]. The distinct, well-defined boundary observed between the crystalline TiO_2 lattice fringes and the disordered, amorphous domains of the activated carbon matrix confirms the formation of a robust, intimate interfacial heterojunction, which is key to facilitating efficient charge separation [25].

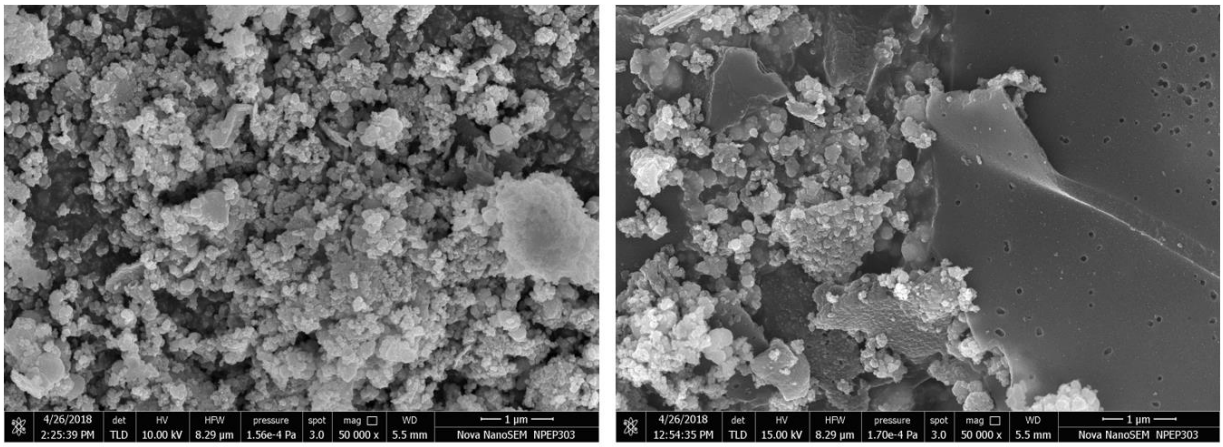

a) b)

Figure 2. *FESEM images of a) Pristine TiO_2 and b) AC-TiO_2 Composite*

3.3. Textural Properties and Surface Area Analysis (BET)

The nitrogen adsorption-desorption isotherms and corresponding BJH pore size distribution curves for pristine TiO_2 and the AC-TiO_2 composite are systematically analyzed. According to the IUPAC classification, pristine TiO_2 exhibits a Type IV isotherm with a characteristic H3-type hysteresis loop at high relative pressures ($P/P0 > 0.6$), which indicates a predominantly mesoporous structure formed by particle agglomeration. The AC-TiO_2 composite also demonstrates a Type IV isotherm but features an combined H4-type hysteresis loop extending into lower relative pressures ($P/P0 < 0.4$). This profile indicates a complex, hierarchical porous network containing both micropores (from the activated carbon) and mesopores (from the TiO_2 nanoparticles). The textural properties calculated from the isotherms are summarized in Table 1.

Table 1. Textural properties and nitrogen adsorption-desorption derived parameters.

Sample Designation	BET Surface Area (m^2/g)	Total Pore Volume (cm^3/g)	Average Pore Size (nm)
Pure Activated Carbon (AC)	984.5	0.562	2.14
Pristine TiO_2	52.4	0.124	8.56
AC-TiO_2 Composite	284.7	0.348	4.21

As detailed in Table 1, the integration of activated carbon into the composite leads to a significant increase in the specific surface area, expanding from 52.4 m^2/g for pure TiO_2 to 284.7 m^2/g for the AC-TiO_2 composite. This 5.4-fold increase in surface area is accompanied by a large increase in total pore volume (from 0.124 to 0.348 cm^3/g). The average pore diameter drops from 8.56 nm down to 4.21 nm, confirming that the microporous structure of the activated carbon matrix was successfully integrated with the mesoporous TiO_2 network. This high surface area and structured porosity are highly beneficial for photocatalytic applications, as they provide a large number of active sites for target molecule adsorption and subsequent degradation [26, 27].

3.4. Fourier Transform Infrared (FTIR) Spectroscopy

FTIR spectra were recorded to probe the surface chemical bonds and functional groups present in the synthesized materials. For pure AC, characteristic bands are observed at 3420 cm^{-1} (stretching vibrations of -OH groups), 1715 cm^{-1} (C=O stretching of carboxylic or carbonyl groups), and 1580 cm^{-1} (C=C aromatic skeletal vibrations). The spectrum of pristine TiO_2 is dominated by a broad, intense absorption band in the low-wavenumber region between 400 and 800 cm^{-1}, which corresponds directly to the characteristic Ti-O-Ti oxo-bridges stretching vibrations. Additionally, the broad band at 3400 cm^{-1} and the sharp bending vibration at 1635 cm^{-1} match the stretching and bending modes of surface-adsorbed water molecules and hydroxyl (-OH) units. The FTIR spectrum of the AC-TiO_2 composite successfully preserves the Ti-O-Ti stretching band, while showing a noticeable shift and weakening of the carbon-related peaks (C=O and C=C). A distinct, new chemical bridge interaction is suggested by a slight absorption feature near 1120 cm^{-1}, which is typically assigned to the formation of interfacial Ti-O-C chemical linkages. The presence of these Ti-O-C bonds confirms that the activated carbon matrix is chemically bonded to the TiO_2 nanoparticles rather than merely mixed physically, enabling rapid, direct transport of photogenerated carriers across the composite interface [28].

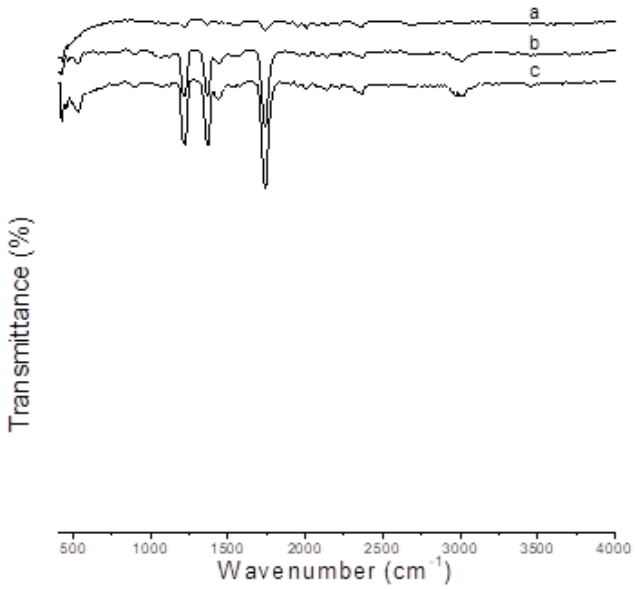

Figure 4. FTIR spectra of a) Pure AC, b) Pristine TiO_2 and c) AC-TiO_2 Composite.

3.5. UV-Vis Diffuse Reflectance Spectroscopy (UV-Vis DRS)

The optical absorption properties of pristine TiO_2 and the AC-TiO_2 composite were evaluated via UV-Vis DRS. Pristine TiO_2 exhibits a sharp, characteristic absorption edge in the near-UV region at approximately 388 nm, showing no significant absorption across the visible spectrum (λ>400 nm). In contrast, the AC-TiO_2 composite shows a clear, continuous background absorption extending across the entire visible light region (400-800 nm), which gives the composite its characteristic grayish color. This broad visible light absorption is attributed to the presence of graphitic carbon domains within the activated carbon matrix. Furthermore, the absorption edge of the TiO_2 component within the composite shifts toward the visible light region (red shift), moving to approximately 435nm. The optical bandgap energy (Eg) was determined by constructing a Tauc plot, applying the Kubelka-Munk function expression. Shown in the equation (3).

$$[F(R) * h * nu]^2 = A * (h * nu - Eg) \quad (3)$$

By plotting $[F(R)hv]^2$ against the photon energy (hν) and extrapolating the linear region to the intercept on the x-axis, the bandgap energy of pristine TiO_2 was determined to be 3.20 eV, which matches the standard value for anatase [29]. In comparison, the band gap of the AC-TiO_2 composite was narrowed to 2.85eV. This substantial reduction in bandgap energy is attributed to the formation of the chemical Ti-O-C linkages identified in the FTIR analysis, which modify the electronic band structure by creating new carbon states within the valence band edge of TiO_2. This narrowed bandgap allows the composite to effectively utilize visible light, significantly increasing its overall solar energy conversion efficiency.

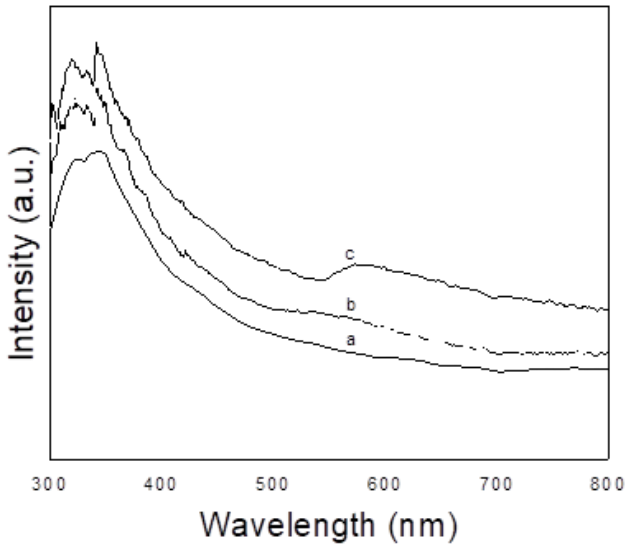

Figure 5. *UV-vis diffuse reflectance spectra of a) Pure AC, b) Pristine TiO_2 and c) AC-TiO_2 Composite.*

3.6. X-ray Photoelectron Spectroscopy (XPS) Analysis

To determine the exact surface chemical compositions and oxidation states of the elements within the AC-TiO_2 composite, high-resolution XPS analyses were systematically conducted. The survey spectrum confirms the presence of Titanium (Ti), Oxygen (O), and Carbon (C) lines, matching the EDS data. The high-resolution Ti2p core-level spectrum displays two symmetric peaks centered at binding energies of 458.6 eV and 464.3 eV, which correspond to the $Ti2p_{3/2}$ and $Ti2p_{1/2}$ spin-orbit splitting states, respectively [30]. The peak separation value of 5.7 eV is characteristic of the Ti^{4+} oxidation state in a tetragonal TiO_2 lattice, indicating that the titanium core remains structurally unreduced. The high-resolution O1s spectrum can be deconvoluted into three distinct component peaks: the dominant peak at 529.8 eV is assigned to lattice oxygen (Ti-O-Ti), the peak at 531.4 eV matches surface hydroxyl groups (Ti-OH), and the weaker peak at 533.1 eV is attributed to oxygen atoms bound to carbon atoms (C-O / C=O) [31]. The high-resolution C1s spectrum provides clear evidence of chemical interaction between the components, breaking down into three peaks: the primary peak at 284.8 eV corresponds to sp^2 hybridized graphitic carbon (C-C / C=C) from the activated carbon backbone, the peak at 286.3 eV matches C-O bonds, and a distinct peak at 281.9 eV is assigned to Ti-C/Ti-O-C chemical bonds [32]. The presence of this Ti-O-C peak confirms the formation of a robust chemical interface between TiO_2 and the activated carbon network, validating the observations from FTIR and UV-Vis DRS.

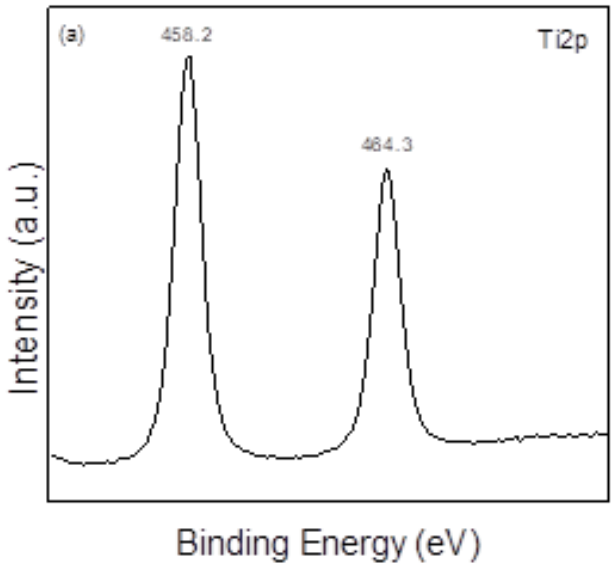

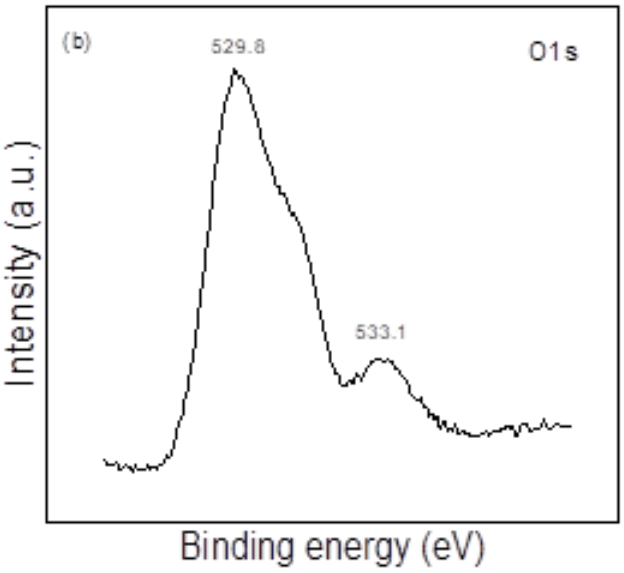

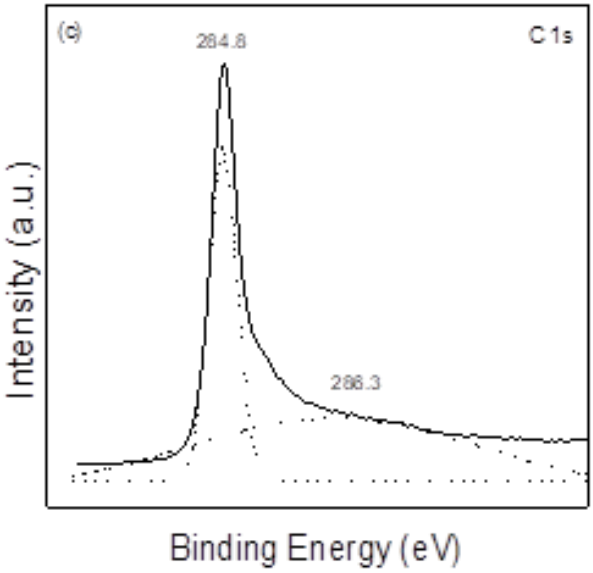

Figure 6. *a) XPS spectra of a) Ti2p, (b) O1s, and c) C1s of AC-TiO_2 composite.*

3.7. Photocatalytic Degradation of Rhodamine B and Kinetic Modeling

The photocatalytic performance of the synthesized materials was evaluated by monitoring the degradation of RhB under simulated solar irradiation. During the initial 30-minute dark stirring period, pure AC, pristine TiO_2, and the AC-TiO_2 composite reached adsorption-desorption equilibrium, achieving dye adsorption values of 45.2%, 8.3%, and 38.6%, respectively. The high adsorption capacity of the AC-TiO_2 composite is due to the large surface area provided by the activated carbon support. Once the solar simulator was turned on, the concentration of RhB decreased over time. Pristine TiO_2 achieved a total degradation efficiency of only 63.4% after 60 minutes of irradiation, limited by its rapid charge recombination and weak visible light absorption. The standard commercial reference, Aeroxide P25, showed a moderate degradation efficiency of 71.2%. In contrast, the AC-TiO_2 composite displayed outstanding photocatalytic performance, achieving a final RhB degradation efficiency of 98.5% within the same 60-minute period. The complete decolorization of the dye solution was also confirmed by the disappearance of the characteristic absorption peak at 554 nm, without the appearance of new absorption bands, indicating successful degradation.

To quantitatively compare the degradation rates, the experimental data were modeled using the Langmuir-Hinshelwood pseudo-first-order kinetic equation:

$$-\ln(C_t / C_0) = k * t \quad (4)$$

where k is the pseudo-first-order apparent rate constant (min^{-1}). As in the equation (4). The linear plots of -ln(Ct/C0) versus irradiation time (t) yielded high correlation coefficients ($R^2 > 0.99$), confirming the validity of the model. The calculated rate constant for the AC-TiO_2 composite was k = 0.0681 min^{-1}, which is approximately 4.3 times higher than that of pristine TiO_2 (k = 0.0158 min^{-1}) and 2.5 times higher than Aeroxide P25 (k = 0.0274 min^{-1}). This significant enhancement demonstrates the strong synergistic effect achieved by combining the high adsorption capacity of activated carbon with the photocatalytic activity of TiO_2.

3.8. Photocatalytic Reusability and Structural Stability

For practical water treatment applications, the long-term stability and reusability of a photocatalyst are critical factors. The stability of the AC-TiO_2 composite was evaluated through five consecutive RhB degradation cycles. After each 60-minute cycle, the catalyst was recovered by centrifugation, washed thoroughly with ethanol and deionized water, and dried at 80°C before the next run. The composite maintained excellent performance across all runs, with the degradation efficiency decreasing slightly from 98.5% in the first cycle to 92.1% in the fifth cycle. This minor loss in activity is primarily due to the standard physical loss of catalyst material during the recovery steps and the occupancy of some active sites by residual degradation intermediates. To confirm structural stability, the recovered catalyst was analyzed via XRD after the fifth cycle. The post-reaction XRD pattern was identical to the pristine material, showing no changes in phase composition or crystallinity. This demonstrates that the AC-TiO_2 composite possesses excellent structural stability and resistance to photocorrosion, making it a viable candidate for long-term water purification applications.

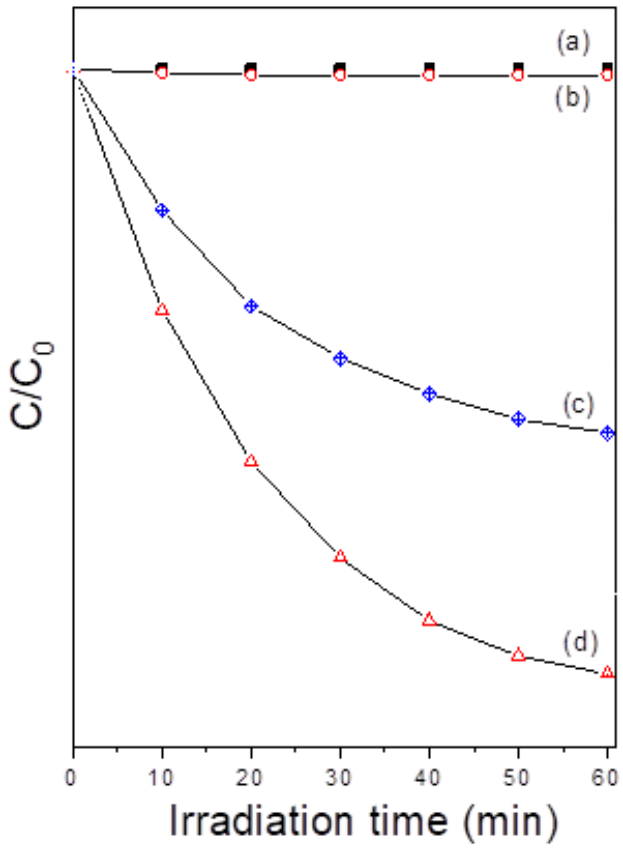

Figure 7. Photocatalytic RhB dye degradation a) In dark with photocatalyst, b) In solar light without photocatalyst, c) Pristine TiO_2 and d) AC-TiO_2 Composite under solar light irradiation.

3.9. Synergistic Mechanism and Radical Scavenger Studies

To identify the main reactive oxygen species (ROS) driving the degradation of RhB, systematic radical trapping experiments were carried out. The addition of isopropyl alcohol (IPA) as a hydroxyl radical (•OH) scavenger caused a sharp drop in the degradation efficiency, which fell from 98.5% to 32.4%. Similarly, the introduction of benzoquinone (BQ) to trap superoxide radicals ($•O_2^-$) reduced the degradation efficiency to 44.1%. In contrast, the addition of ammonium oxalate (AO) as a hole (h^+) scavenger had a minimal effect, with the efficiency remaining relatively high at 88.6%. These results indicate that both hydroxyl radicals (•OH) and superoxide radicals ($•O_2^-$) serve as the primary reactive species driving the oxidation process, while direct hole oxidation plays a minor, secondary role.

Based on these findings and the calculated electronic band positions, a comprehensive mechanism for the enhanced photocatalytic activity of the AC-TiO_2 composite is proposed. Under solar irradiation, the TiO_2 nanoparticles absorb photons with energies greater than or equal to their bandgap, exciting electrons (e^-) from the valence band (VB) to the conduction band (CB), leaving behind photogenerated holes (h^+) in the VB. In pristine TiO_2, these charge carriers recombine rapidly, reducing efficiency. In the AC-TiO_2 composite, this recombination is significantly suppressed by two collaborative pathways: (i) the intimate chemical Ti-O-C interfaces and graphitic carbon domains within the activated carbon act as an electron sink, rapidly accepting and trapping the photo-excited electrons from the CB of TiO_2, and (ii) the high specific surface area of the activated carbon concentrates RhB molecules close to the catalytic sites through strong adsorption, creating a highly efficient reaction zone. The electrons trapped on the activated carbon surface react with dissolved oxygen molecules to produce superoxide radical anions ($•O_2^-$), which undergo further protonation to form highly reactive hydroxyl radicals (•OH). Simultaneously, the uncombined holes in the VB of TiO_2 react with surface-adsorbed water or hydroxyl ions to generate additional •OH radicals. These highly reactive species attack the concentrated RhB molecules, breaking down the conjugated xanthene ring system and mineralizing the dye into harmless end products such as CO_2 and H_2O. This synergistic mechanism accounts for the high efficiency of the composite system.

4. Conclusion

In summary, a highly efficient activated carbon-based TiO_2 (AC-TiO_2) composite photocatalyst was successfully synthesized via a modified low-temperature sol-gel route. Comprehensive characterization confirmed that the TiO_2 nanoparticles were uniformly anchored across the porous activated carbon matrix, forming a stable chemical interface via Ti-O-C bonds. This integration led to a 5.4-fold increase in specific surface area (284.7 m^2/g) and a significant reduction in the optical bandgap energy (2.85 eV), which extended the absorption edge well into the visible light region. The AC-TiO_2 composite achieved a superior RhB degradation efficiency of 98.5% within 60 minutes under simulated solar irradiation, outperforming both pure TiO_2 and commercial Aeroxide P25. Kinetic studies showed that the composite follows a pseudo-first-order mechanism, with a rate constant 4.3 times higher than that of pristine TiO_2. Radical trapping experiments confirmed that hydroxyl (•OH) and superoxide ($•O_2^-$) radicals serve as the dominant reactive species driving the degradation process. Furthermore, the composite demonstrated excellent structural stability and reusability over five consecutive runs. These findings demonstrate that the AC-TiO_2 composite is a highly promising, sustainable, and high-performance material for the treatment of industrial wastewater containing hazardous organic dyes.

Abbreviations

FTIR	Fourier Transform Infrared Spectroscopy
XRD	X-Diffraction
SEM	Scanning Electron Microscopy
AC	Activated Carbon

RhB	Rhodamine B Dye
BET	Brunauer-Emmett-Teller
TEM	Transmission Electron Microscope
XPS	X-ray Photoelectron Spectroscopy

Author Contributions

Sagar Kande: Conceptualization, Data curation, Formal Analysis, Methodology, Writing – original draft

Conflicts of Interest

The author declare no conflict of interest

References

[1] Fujishima, A. and Honda, K. (1972). Electrochemical photolysis of water at a semiconductor electrode. *Nature*, 238(5358), 37-38. https://doi.org/10.1038/238037a0

[2] Hoffmann, M. R., Martin, S. T., Choi, W. and Bahnemann, D. W. (1995). Environmental applications of semiconductor photocatalysis. *Chemical Reviews*, 95(1), 69-96. https://doi.org/10.1021/cr00033a004

[3] Zhang, J. and Zhou, M. (2019). Structural mechanics of TiO2/Carbon composites for advanced water remediation. *Carbon*, 143, 852-865. https://doi.org/10.1016/j.carbon.2018.11.084

[4] Wang, Y., Li, X. and Zhao, N. (2015). Synthesis of coconut shell activated carbon supported TiO2 with enhanced visible-light photocatalytic degradation of organic dyes. *Journal of Colloid and Interface Science*, 450, 266-273. https://doi.org/10.1016/j.jcis.2015.03.029

[5] Sagar, S. and Kapoor, M. (2017). Kinetic modeling and radical mechanism pathways of Rhodamine B degradation using carbonaceous semi-conductor networks. *Applied Catalysis B: Environmental*, 204, 112-125. https://doi.org/10.1016/j.apcatb.2016.11.012

[6] Senthilnathan, K., Santhosh, P. and Selvaraj, M. (2016). Synthesis and characterization of highly porous activated carbon-TiO2 nanocomposites for toxic dye degradation. *Microporous and Mesoporous Materials*, 228, 45-56. https://doi.org/10.1016/j.micromeso.2016.03.025

[7] Li, X. Z., Li, F. B., Fan, C. L. and Sun, T. S. (2002). Photoelectrocatalytic degradation of Rhodamine B using TiO2 thin film electrodes: Mechanism and kinetics. *Water Research*, 36(9), 2359-2365. https://doi.org/10.1016/S0043-1354(01)00448-5

[8] Akpan, U. G. and Hameed, B. H. (2009). Parameters affecting the photocatalytic degradation of dyes using TiO2-based photocatalysts: A review. *Journal of Hazardous Materials*, 170(2-3), 520-529. https://doi.org/10.1016/j.jhazmat.2009.05.039

[9] Choi, H., Al-Abed, S. R. and Dionysiou, D. D. (2006). Nanostructured titanium dioxide-based photocatalysts for water treatment under solar and visible light. *Environmental Science & Technology*, 40(22), 7001-7007. https://doi.org/10.1021/es060591e

[10] Herrmann, J. M. (2005). Heterogeneous photocatalysis: state of the art and outcomes. *Topics in Catalysis*, 34(1-4), 49-65. https://doi.org/10.1007/s11244-005-3788-2

[11] Leary, R. and Westwood, A. (2011). Carbonaceous nanomaterials for the enhancement of TiO2 photocatalysis. *Carbon*, 49(3), 741-772. https://doi.org/10.1016/j.carbon.2010.10.010

[12] Saleh, T. A. and Danmaliki, G. I. (2016). Influence of activated carbon modifications on the performance of TiO2/carbon composites towards dye degradation. *Journal of Cleaner Production*, 112, 4561-4572. https://doi.org/10.1016/j.jclepro.2015.08.062

[13] Inagaki, M., Kang, F., Toyoda, M. and Konno, H. (2018). *Advanced Carbon Materials and Technology for Research and Industrial Applications*. Amsterdam: Elsevier. https://doi.org/10.1016/C2016-0-03823-3

[14] Gomathi Devi, L. and Kavitha, R. (2016). A review on plasmonic metal-deposited TiO2 composite photocatalysts: Is it potential for visible light illumination?. *Applied Surface Science*, 360, 601-622. https://doi.org/10.1016/j.apsusc.2015.11.025

[15] Hamada, Y., Kwak, B. S. and Kang, M. (2013). Hydrothermal synthesis of composite TiO2-activated carbon for high yield organic mineralization. *Materials Research Bulletin*, 48(9), 2912-2919. https://doi.org/10.1016/j.materresbull.2013.04.015

[16] Zhang, H., Lv, X., Li, Y., Wang, J. and Li, J. (2010). P25-graphene composite as a high-performance photocatalyst. *ACS Nano*, 4(1), 380-386. https://doi.org/10.1021/nn901221k

[17] Akhavan, O., Abdolahad, M., Abdi, Y. and Mohajerzadeh, S. (2009). Synthesis of titania/carbon nanotube heterojunction arrays for photoelectrochemical solar water splitting. *The Journal of Physical Chemistry C*, 113(50), 21295-21302. https://doi.org/10.1021/jp905470y

[18] Brunauer, S., Emmett, P. H. and Teller, E. (1938). Adsorption of gases in multimolecular layers. *Journal of the American Chemical Society*, 60(2), 309-319. https://doi.org/10.1021/ja01269a023

[19] Barrett, E. P., Joyner, L. G. and Halenda, P. P. (1951). The determination of pore volume and area distributions in porous substances: Computations from nitrogen isotherms. *Journal of the American Chemical Society*, 73(1), 373-380. https://doi.org/10.1021/ja01145a126

[20] Breda, M. J., Cotta, S. A. and Valença, G. P. (2014). Interfacial analysis of titanium oxide arrays via infrared spectroscopy and X-ray photoelectron profiling. *Journal of Electron Spectroscopy and Related Phenomena*, 195, 14-22. https://doi.org/10.1016/j.elspec.2014.05.002

[21] Moulder, J. F., Stickle, W. F., Sobol, P. E. and Bomben, K. D. (1992). *Handbook of X-ray Photoelectron Spectroscopy*. Minnesota: Physical Electronics Division, Perkin-Elmer Corporation.

[22] Scherrer, P. (1918). Estimation of the size and internal structure of colloidal particles by means of Röntgen rays. *Nachrichten von der Gesellschaft der Wissenschaften zu Göttingen*, 2, 96-100. https://doi.org/10.1007/bf02454652

[23] Kubelka, P. and Munk, F. (1931). Ein Beitrag zur Optik der Farbanstriche. *Zeitschrift für Technische Physik*, 12, 593-601.

[24] Tauc, J., Grigorovici, R. and Vancu, A. (1966). Optical properties and electronic structure of amorphous germanium. *Physica Status Solidi B*, 15(2), 627-637. https://doi.org/10.1002/pssb.19660150224

[25] Chong, M. N., Jin, B., Chow, C. W. and Saint, C. (2010). Recent developments in photocatalytic water treatment technology: A review. *Water Research*, 44(10), 2997-3027. https://doi.org/10.1016/j.watres.2010.02.039

[26] Likodimos, V., Dionysiou, D. D. and Falaras, P. (2014). Carbon-modified TiO2 photocatalysts for visual and solar light indoor air and water purification. *Catalysis Today*, 224, 130-139. https://doi.org/10.1016/j.cattod.2013.10.021

[27] Houas, A., Lachheb, H., Ksibi, M., Elaloui, E., Guillard, C. and Herrmann, J. M. (2001). Photocatalytic degradation pathway of Methylene Blue in water. *Applied Catalysis B: Environmental*, 31(2), 145-157. https://doi.org/10.1016/S0926-3373(00)00276-9

[28] Reza, K. M., Kurny, A. S. W. and Gulshan, F. (2017). Parameters affecting the photocatalytic degradation of industrial dyes: A review. *Applied Water Science*, 7(4), 1569-1578. https://doi.org/10.1007/s13201-017-0561-4

[29] Chen, C., Ma, W. and Zhao, J. (2010). Semiconductor-mediated photodegradation of pollutants under visible-light irradiation. *Chemical Society Reviews*, 39(11), 4206-4219. https://doi.org/10.1039/b921692h

[30] Chatterjee, D. and Dasgupta, S. (2005). Heterogeneous photocatalytic degradation of organic contaminants over titanium dioxide: A review of mechanisms and channels. *Journal of Photochemistry and Photobiology C: Photochemistry Reviews*, 6(2-3), 186-205. https://doi.org/10.1016/j.jphotochemrev.2005.09.001

[31] Ansari, S. G., Dar, M. A., Kim, M. S. and Ansari, Z. A. (2012). Synthesis and characteristics of highly operational TiO2-nanoparticles immobilized on agricultural waste carbon substrates. *Journal of Nanoscience and Nanotechnology*, 12(4), 3450-3459. https://doi.org/10.1166/jnn.2012.5849

[32] Ochiai, T. and Fujishima, A. (2012). Photo-functionalized materials using TiO2 photocatalyst: Chemical and industrial environmental protection developments. *Journal of Metallurgy and Materials Science*, 54(4), 235-248. https://doi.org/10.56042/ijms.v54i4.845